Revision 1

Viscosity of Earth's inner core constrained by Fe–Ni interdiffusion in Fe–Si alloy in an internal-resistive-heated diamond anvil cell

Yohan Park[1], Kyoko Yonemitsu[2], Kei Hirose[2,3], Yasuhiro Kuwayama[2], Shintaro Azuma[1], and Kenji Ohta[1,*]

[1]Department of Earth and Planetary Sciences, Tokyo Institute of Technology, Tokyo 152-8551, Japan

[2]Department of Earth and Planetary Science, The University of Tokyo, Tokyo 113-0033, Japan

[3]Earth-Life Science Institute, Tokyo Institute of Technology, Tokyo 152-8550, Japan

*Corresponding author.

E-mail address: k-ohta@geo.titech.ac.jp (K. Ohta).

ABSTRACT

Diffusivity in iron (Fe) alloys at high pressures and temperatures imposes constraints on transport properties of the inner core, such as viscosity. Because silicon (Si) is among the most likely candidates for light elements in the inner core, the presence of Si must be considered when studying diffusivity in the Earth's inner core. In this study, we conducted diffusion experiments under pressure up to about 50 GPa using an internal-resistive-heated diamond anvil cell (DAC) that ensures stable and homogeneous heating compared with a conventional laser-heated DAC and thus allows us to conduct more reliable diffusion experiments under high pressure. We determined the coefficients of Fe–nickel (Ni) interdiffusion in the Fe–Si 2 wt.% alloy. The obtained diffusion coefficients follow a homologous temperature relationship derived from previous studies without considering Si. This indicates that the effect of Si on Fe–Ni interdiffusion is not significant. The upper limit of the viscosity of the inner core inferred from our results is low, indicating that the Lorentz force is a plausible mechanism to deform the inner core.

Keywords: Earth's inner core, diffusion, viscosity, iron, silicon, high pressure

INTRODUCTION

Viscosity is a crucial physical property to understand dynamical processes in planetary interiors. The viscosity of the Earth's inner core constrains the modes and mechanisms of viscous flows responsible for the observed seismic anisotropy of the inner core (Lasbleis and Deguen 2015). Seismological observations of the inner core reveal its complicated anisotropic structures; the P wave travels ~3–4% faster along the polar direction compared to its equatorial direction (e.g., Poupinet et al. 1983). This anisotropy of the inner core can be attributed to lattice preferred orientation (LPO) induced by the viscous flow of inner core materials (Deguen 2012; Romanowicz and Wenk 2017). The Rayleigh–Bénard convection was first proposed as a possible mechanism of viscous flow in the inner core (Jeanloz and Wenk 1988). Yoshida et al. (1996) argued that the inner core grows preferentially to the equatorial direction due to the columnar convection of the outer core. Such heterogeneous inner core growth leads to isostatic disequilibrium, and the resultant differential stress gives rise to a viscous flow in the inner core. External forces related to the Earth's magnetic field, such as the Lorentz force, or force induced by heterogeneous joule heating, have been proposed as possible mechanisms for the viscous flow in the inner core (Karato 1999; Takehiro 2011). The strength and mode of viscous flows (i.e., the plausibility of the proposed mechanisms) heavily depend on the viscosity of the inner core; however, there is significant uncertainty in its estimates, which range from 10^{10} Pa s to 10^{22} Pa s (Buffett 1997; Davies et al. 2014; Frost et al. 2021; Jackson et al. 2000; Koot and Dumberry 2011; Reaman et al. 2011; Ritterbex and Tsuchiya 2020; Van Orman 2004; Yoshida et al. 1996). These studies estimated the viscosity of the inner core either from experiments, *ab initio* calculations, or geophysical observations.

From a mineral physics point of view, the approach often adopted is an estimate of the viscosity based on the diffusion coefficient of iron (Fe) under high pressure (Yunker and Van Orman 2007; Reaman et al. 2012; Ritterbex and Tsuchiya 2020). Terrestrial cores are thought to be composed of Fe alloyed with nickel (Ni) and some light elements. Solid Fe alloys composing the Earth's inner core assume a hexagonal closed packed (hcp) structure, while pressure and temperature conditions of the centers of smaller terrestrial planets, such as Mercury and Mars, favor face-centered cubic (fcc) structures of iron alloys as a dominant phase of their possible solid inner cores, depending on light element concentrations

(Komabayashi et al. 2019; Tsujino et al. 2013). Although the self-diffusivity of Fe under high pressure is a critical limiting factor of crystal plasticity of inner core materials, the self-diffusion coefficient of Fe under pressures relevant to the deep Earth has not been studied experimentally due to experimental difficulties. Instead, experimental attempts have been made to estimate the effects of pressure on Fe–Ni interdiffusion coefficients as an analogy of Fe self-diffusion coefficients (Reaman et al. 2012; Yunker and Van Orman 2007).

An open question unaddressed by previous studies is the effect of light elements on Fe–Ni interdiffusion coefficients, as the Earth's inner core must contain ~1–3 wt.% light elements (Badro et al. 2007; Fei et al. 2016). In such alloys, the diffusivity of solvent atoms (Fe in this case) is subject to change by the presence of solute elements. One of the likely light elements to explain the density deficit and velocity reduction of the inner core with respect to pure Fe is silicon (Si) (Antonangeli et al. 2010; Mao et al. 2012; Sakairi et al. 2018). Therefore, the diffusivity in Fe–Si alloys under high pressure is of great importance for estimating diffusivity in the Earth's inner core.

In this study, we conducted Ni diffusion experiments on an Fe–2 wt.% Si alloy to study the effect of Si on the Fe–Ni interdiffusion coefficient for pressures up to ~50 GPa. We used an internal-resistive-heated DAC (IRHDAC), where the sample is heated with smaller temperature gradients and lower temporal fluctuations than in the conventional laser-heated DAC (LHDAC). We compare our results with previous studies on the Fe–Ni interdiffusion coefficient (Reaman et al. 2012; Yunker and Van Orman 2007) and further discuss its implications on the diffusivity and viscosity of the Earth's inner core.

EXPERIMENTAL METHODS

We prepared diffusion couples by coating a thin film of Ni (3N purity level) on foils of the Fe–2 wt.% Si alloy using a magnetron sputtering system. The thickness of the coated Ni layer is approximately 300 nm. The Ni coated Fe–Si foils were further fabricated by a focused ion beam (FIB) apparatus (FEI Versa 3D) to make diffusion couples whose size fits the sample chamber of a DAC. We place the prepared diffusion couple into an IRHDAC with single-crystal sapphire and alumina powder as pressure medium and thermal insulator against diamond anvils (Fig. 1). We used diamond anvils with a culet size of 300 μm for pressure generation. The surface of the preindented Re gasket was electrically insulated by cBN+TiO_2 powder and cement (Resbond^{TM} 919), similarly to the literature (Inoue et al. 2020; Suehiro et al. 2019). Two Pt foils on the insulation layer act as electrical leads connecting the Ni+Fe–Si diffusion couple inside the sample chamber and Cu wires outside of the gasket, which creates a circuit for resistive heating of the diffusion couple itself.

After compression to the pressure of interest, electricity was supplied to the diffusion couple from a DC electric power supply (TAKASAGO ZX-400LA) through the prepared circuit. The temperature of diffusion couple during joule heating is determined from the thermal radiation spectrum to fit Planck's law. The thermal radiation emitted from the heated sample is collected through the refractive lens and reflected by dichroic and silver mirrors, and finally was recorded with a Princeton grating spectrometer combined with a CCD array detector. The system optical response was calibrated with a certified tungsten lamp. For the data reduction, we used the LightField software package. Target temperatures were reached within 10 seconds and maintained during diffusion experiments (Table 1). The temperature error from fitting of a spectrum is typically less than 0.3%. 1-dimensional temperature distributions of the specimens were obtained (Fig. 2) and errors of our temperature measurements are estimated from standard deviation of the temporal and radial temperature fluctuation of the specimens. After diffusion experiments, the specimens were quenched rapidly by shutting off the electric power supply. Pressures inside the sample chamber were determined by the Raman shift of a diamond anvil (Akahama and Kawamura 2006), and thermal pressure during heating was corrected using an estimation from Sinmyo et al. (2019). The overall uncertainty in pressure may be less than 5%.

After the diffusion experiments, samples were recovered to ambient condition, and thin cross-sections across the heated region of the diffusion couple were prepared by FIB for transmission electron microscope (TEM) analysis. We further conducted microstructural observations and chemical analysis during sample preparation using the scanning ion microscope (SIM) and energy dispersive X-ray spectroscopy (EDS) mounted on the FIB apparatus. After sample preparation, microstructural observations and chemical analysis were conducted using TEM (JEOL JEM-2800). The acceleration voltage was 200 kV, and the probe size was about 1.0 nm.

RESULTS AND DISCUSSION

We performed four separate diffusion experiments, in which pressure–temperature conditions were in the stability field of the fcc phase of Fe–2 wt.% Si alloy according to Komabayashi et al. (2019) (Table 1). Temperature variations along the radial direction of the heated area were at most ~50 K (Fig. 2). Moreover, the temperature difference between both sides of the specimen and temperature fluctuation during the diffusion experiment was at most ~100 K. The temperature homogeneity and heating stability of our method were significantly improved compared to LHDAC (Reaman et al. 2012), and thus desirable for precise diffusion experiments.

The SIM observation during FIB cross-sectioning allows us to observe grain boundaries in the specimen after the diffusion experiment (Fig. 3a). The SIM images show the boundary between Fe–Si alloy and thin Ni layer and it can be observed that thickness of the Ni layer is reduced from initial ~300 nm to 100-150 nm after high-pressure experiment (Fig. 3a). The sample texture shown in Fig. 3a can be attributed to the phase transformation of Fe alloys from fcc to hcp after the temperature quench and the martensitic phase transformation from hcp to bcc during decompression. Large domains having a similar orientation of twin boundaries can be considered as former fcc grains during diffusion experiments. Domains of former fcc grains have sizes of several micrometers at the central part of the specimen, whereas grains have finer sub-micrometer sizes at the sample corners in contact with Pt electrodes. This grain size distribution in the specimen suggests grain growth of Fe alloys during diffusion experiments. Element mapping of the sample cross-sections obtained by EDS indicates the existence of high-diffusivity paths in the specimens, and the paths match boundaries of large domains observed in the SIM image, which is evidence of grain boundary diffusion (Fig. 3b). Contamination of specimens from Pt electrodes would be negligible as temperature of areas having contacts with Pt electrodes are relatively low. We also confirmed that there is no significant contamination of specimens from Pt electrodes after heating for 3 hours under 1900 K and 40 GPa.

We further conducted TEM-EDS elements mapping analyses for all specimens and confirmed that the grain boundary diffusion is active in our experiments (Fig. 4). In some regions, Fe diffusion into grain boundaries of the Ni layer is also observed (Fig. 4c). Since the focus of this study is to determine lattice diffusion coefficient of Fe–Ni interdiffusion, the

TEM-EDS point analyses were performed in several areas within the quenched sample along lines perpendicular to the diffusion boundary, avoiding areas of significant grain boundary diffusion, based on Ni element mapping results (FIGURE 4b). Furthermore, diffusion profiles with evidence of grain boundary diffusion were excluded from the obtained line profile results. Fig. 5 shows two representative diffusion profiles obtained from separate experiments. The measurement error of Ni concentration is evaluated by the variation of the value of the diffusion profile obtained within the same sample, and it was found that the Ni concentration has a maximum error of only 2%. Although Run #2 experienced a shorter heating duration compared with Run #3, higher temperature and lower-pressure condition of Run #2 during the diffusion experiment makes its diffusion distance longer than that of Run #3. This reduction in the diffusion distance with increasing pressure and decreasing temperature is consistent with the known pressure and temperature dependence of diffusion (Mehrer 2007). The TEM-EDS analyses confirmed that the quenched samples had a Si content of 2 wt.%, the same composition as the starting material.

The diffusion of particles inside an anisotropic medium can be described by following Fick's second law:

$$\frac{\partial C}{\partial t} = \nabla \cdot (D \nabla C), \qquad (1)$$

where *C* is concentration of diffusion particles, *D* is diffusion coefficient, and *t* is time during which the diffusion has been taking place. Due to the limited sample sizes in this study, it is challenging to evaluate concentration dependence on diffusion coefficient. If we ignore the concentration effect on diffusivity, we can express Eq. (1) as Eq. (2):

$$\frac{\partial C}{\partial t} = D \Delta C. \qquad (2)$$

Because we have a thin layer of Ni (having thickness of 100-150 nm) as tracers in our experiments, it is appropriate to apply the 'thin film geometry' (Crank 1975). Applying the thin film geometry to Eq. (2) yields the following 'thin film solution':

$$\mathrm{C(x,t)} = \frac{M}{\sqrt{\pi D t}} \exp(-\frac{x^2}{4Dt}), \qquad (3)$$

where *M* is the initial amount of the tracer, and x is diffusion distance.

We apply the thin film solution to the diffusion profiles obtained in this study (Fig. 5).

Multiple diffusion profiles obtained at several different regions were used to estimate the diffusion coefficients. We calculated the averages of diffusion coefficients estimated from diffusion profiles and used their standard deviation as the estimated error (Table 1). To validate the use of the thin film solution, we performed finite element method (FEM) analysis on diffusion in Run #3 by using commercial software COMSOL Multiphysics (COMSOL Inc.) (Fig. 6a). We assume diffusion of tracers having thickness of 120 nm for 400 seconds with diffusion coefficient of 4.08×10^{-17} m^2 s^{-1} estimated from the thin film solution. The result of finite element analysis reasonably reproduces the experimentally observed diffusion profile and support validity of using the thin film solution to estimate diffusion coefficients in this study (Fig. 6b).

Because the kinetics of diffusion are dictated by the thermal vibration of atoms, the diffusion coefficient can frequently be expressed by the following Arrhenius formula:

$$\mathrm{D} = D_0 \exp\left(-\frac{E_A+PV_A}{RT}\right), \tag{4}$$

where E_A is the activation energy, P is the pressure, V_A is the activation volume, R is the gas constant, T is the temperature, and D_0 is a pre-exponential factor. According to Eq. (4), activation volume V_A can be derived from the slope of the logarithm of diffusion coefficients against pressure. We plotted the diffusion coefficients at similar temperature conditions against pressure and derived the activation volume using Eq. (4) (Fig. 7). Present diffusion coefficients are consistent with the linear fit line suggested by Yunker and Van Orman (2007) and relatively low compared to other fits, including the result of Reaman et al. (2012). While Yunker and Van Orman (2007) suggests the activation volume of 3.1±0.7 cm^3 mol^{-1} under a pressure of ~23 GPa, Reaman et al. (2012) suggests a decrease in the activation volume to 2.62 cm^3 mol^{-1} at 65 GPa. The decrease in the activation volume with increasing pressure is anticipated with the homologous temperature relationship and our current understanding of the high-pressure melting curve of Fe. However, the results of Reaman et al. (2012) might contain systematic errors in the temperature measurement, as they used LHDAC showing large temperature gradients and possible unstable heating. In contrast, a multi-anvil apparatus and a piston-cylinder apparatus employed by Yunker and Van Orman (2007) exhibit a rather homogeneous temperature distribution, high stability, and accuracy in the temperature measurement compared to LHDAC. The activation volume estimated solely from our results is 3.49±0.3 cm^3 mol^{-1}, which is consistent with the experimental result of Yunker and Van Orman (2007), and equal to their theoretical prediction based on the homologous scaling. Our results suggest that the diffusion process and lattice geometry of the specimens in this study approximately identical to those obtained in previous studies on Fe–Ni interdiffusion, and the effects of 2 wt.% of Si on Fe–Ni interdiffusion is negligible.

Previous studies suggested that the 'homologous temperature relationship' worked under high-pressure conditions:

$$D = D_0 exp(-\frac{AT_m}{RT}), \tag{5}$$

where A is an empirical constant, and T_m is the melting temperature. We plotted diffusion coefficients against the homologous temperature estimated from the melting temperature of Fe reported by Sinmyo et al. (2019) (Fig. 8). We use the melting temperature of pure Fe, as the incorporation of 2 wt.% of Si into Fe does not decrease the melting temperature significantly (e.g., Fischer et al. 2013; Komabayashi 2020). The plots of our data and Yunker and Van Orman (2007) follow homologous temperature relationships suggested in previous studies under lower pressure regimes (Goldstein et al. 1965; Ritterbex and Tsuchiya 2020). The results of Reaman et al. (2012) also seem to be consistent with other studies, although the results of Reaman et al. (2012) show slight deviations from the trend, probably due to relatively large temperature uncertainties originated from LHDAC. The slope represents empirical constant A/R in Eq. (5), which depends on the crystal structure and bonding properties. A/R derived from this study is 20.37, while Yunker and Van Orman (2007) and Reaman et al. (2012) report 20.4 and 19.3, respectively. Considering the temperature and pressure conditions of diffusion experiments in this study and that of Yunker and Van Orman (2007), the specimens in both studies were assumed to be the fcc structure. Further, we can assume that the bonding properties of Fe–2 wt.% Si alloy are not significantly different from that of pure Fe, as alloying of 2 wt.% of Si does not change the melting temperature significantly (e.g., Fischer et al. 2013; Komabayashi 2020). Therefore, we conclude that Ni diffusion in Fe–2 wt.% Si would show a similar slope to the result of the previous study on Fe–Ni interdiffusion (Yunker and Van Orman 2007). Our estimation of the diffusion coefficient in the inner core is $3.29(\pm1.55)\times10^{-14}$ m^2 s^{-1}, assuming T_m/T of the Earth's inner core is 1.05 (Reaman et al. 2012). As shown by Yunker and Van Orman (2007), there are cases where concentration dependence exists in Fe–Ni interdiffusion. However, since the results of our FEM analysis without considering the concentration dependence are in good agreement with the experimental data (Fig. 6), the effect of the concentration dependence of Fe–Ni interdiffusion would be small under our experimental conditions. The concentration dependence of Fe–Ni interdiffusion decreases with increasing temperature up to about 2000 K at the equivalent pressures (Yunker and Van Orman 2007). Therefore, the concentration dependence of the diffusion coefficient is not expected to have a significant effect under high temperature conditions such as those in the Earth's inner core.

The Fe–Si alloy containing up to 7 wt.% Si has a hcp structure under pressure and temperature conditions relevant to the inner core (Tateno et al. 2015). Because 7 wt.% Si is more than sufficient to explain the density deficit of the inner core, and the Si composition in the inner core is thought to be ~1–2 wt.% (Antonangeli et al. 2010; Badro et al. 2007; Sakairi et al. 2018), the inner core is still expected to be composed of Fe alloys having a hcp structure, even when taking into account the presence of Si. Even though we conducted experiments under pressure and temperature conditions of the fcc stable region according to previous studies (Fischer et al. 2013; Komabayashi et al. 2020), our result can be applied to the Earth's inner core, as the diffusivity in the fcc crystal would be similar to that in hcp crystal, because they both assume the closest packed structure. Indeed, numerous hcp and fcc metals show comparable diffusion coefficients at the same homologous temperatures (Brown and Ashby 1980). The inner core also likely contains some amount of light elements other than Si such as S, O, C, and H (Hirose et al. 2021). Effects of the presence of theses multiple light elements on diffusivity in the inner core should be further studied.

IMPLICATION: ESTIMATION OF UPPER LIMIT OF EARTH'S INNER CORE VISCOSITY

The seismic anisotropy of the Earth's inner core can be interpreted as a result of viscous flow that induces LPO of the inner core material (Deguen 2012; Romanowicz and Wenk 2017). Various models have been suggested for explaining the viscous flow in the Earth's inner core (Buffett and Bloxham 2000; Jeanloz and Wenk 1988; Karato 1999; Takehiro 2011; Yoshida et al. 1996), and the plausibility of each model depends on the viscosity of the

Earth's inner core, which can be evaluated from mechanical properties and diffusion coefficient of the inner core material. Herein, we use the diffusion coefficient estimated in this study to place a constraint on the upper limit of the viscosity of the Earth's inner core. If the seismic anisotropy can be attributed to the LPO of Fe alloys induced by deformation, the active creep mechanism in the inner core would be dislocation-controlled creep, rather than diffusion creep, as the latter may not develop LPO or rather destroy pre-existing LPO (Boullier and Gueguen 1975). Moreover, all previous studies on the grain size of the inner core support a large grain size, which makes diffusional creep of the inner core infeasible. Considering low seismic attenuation of the inner core, its grain size might be within a range of 10^2–10^3 m (Cormier and Li 2002). Grain growth experiments on hcp Fe under high pressure suggest the inner core grain size ranging from several hundred meters to several kilometers (Yamazaki et al. 2017). Irrespective of the above-mentioned estimation adopted, diffusional creep will lead to a notably high viscosity of the inner core ranging from ~10^{24} to 10^{27} Pa s (Ritterbex and Tsuchiya 2020). This estimation is higher than the upper end of the range of previously estimated viscosity (Buffett 1997; Davies et al. 2014; Frost et al. 2021; Jackson et al. 2000; Koot and Dumberry 2011; Reaman et al. 2011; Ritterbex and Tsuchiya 2020; Van Orman 2004; Yoshida et al. 1996), which in turn makes dislocation-based creep the dominant creep mechanism.

Based on the high homologous temperature and low-stress condition of the inner core, Harper-Dorn creep has been suggested as a controlling creep mechanism in the inner core (Van Orman 2004). Harper-Dorn creep is a dislocation-based mechanism that has been reported in experimental studies under low deviatoric stress and high homologous temperature conditions (Harper and Dorn 1957), similar to those in the inner core. However, this has been observed only in high purity metals, while the inner core includes around 5% Ni and a certain number of light elements. Further, its underlying physical mechanisms and even its existence remain controversial (Blum et al. 2002).

Among dislocation-based creep mechanisms, the most widely accepted one is the power law creep:

$$\dot{\varepsilon} = \alpha \frac{DGb}{kT} \left(\frac{\sigma}{G}\right)^n, \tag{6}$$

where $\dot{\varepsilon}$ is the strain rate, α is a constant, D is the diffusion coefficient, G is the shear modulus, b is the burgers vector, k is the Boltzmann constant, σ is the differential stress, and n is the stress exponent. Viscosity (η) is defined as an equation:

$$\eta = \frac{\sigma}{2\dot{\varepsilon}}. \tag{7}$$

With a T_m/T lower than 2.5, the creep mechanism suggested by Weertman (1957) may be active, which assume dislocation glide produces strain and dislocation climb is the rate limiting process. Weertman's creep can be expressed by n = 3 and stress-dependent parameter α, depending on the lattice plane distance d between slip planes (Ritterbex and Tsuchiya 2020). We employ the basic assumptions of Ritterbex and Tsuchiya (2020) and calculate the upper limit of viscosity in the Earth's inner core. For the diffusion coefficient, we used 3.29(±1.55)×10^{-14} m^2 s^{-1} derived from the present results (Fig. 8). For lattice parameters a and c of hcp Fe at the inner core conditions, we use experimental results by Tateno et al. (2010). We employ the shear modulus of 212 GPa (Vočadlo et al. 2009) and assume that a basal slip of hcp Fe is active in the inner core conditions (hence, $b = a$ and $d = c/2$).

To estimate the maximum viscosity of the inner core, we first define the minimum strain rate in the inner core that develops its deformation-induced anisotropy. Nishihara et al. (2018) conducted shear deformation experiments on hcp Fe, which revealed that the texture development was initiated at a strain of 0.5. If we assume that the viscous flow has been active since the beginning of the inner core formation, the strain of 0.5 divided by the inner core age would yield the minimum strain rate $\dot{\varepsilon}$ for explaining deformation-induced anisotropy in the inner core. Recent estimates on mantle global circulation heat flow suggest the inner core age ranging from ~400 to ~1100 Ma (Olson et al. 2015). The anomalously low Ediacaran paleomagnetic field intensity suggests the onset of inner core growth at around ~500 Ma (Bono et al. 2019). Core thermal conductivity estimated from high-pressure experiments also can constrain inner core age to be ~700 Ma (Ohta et al. 2016). Here, we employ the inner core age of 1100 Ma for conservative estimation, thus the minimum strain rate of the inner core would be 1.44×10^{-17} s^{-1}. We then substitute the estimated minimum strain rate and relevant physical parameters into Eq. (6) to derive minimum stress conditions σ in the inner core. The minimum stress condition of the inner core would be around 0.12 Pa when using the diffusion coefficient estimated in this study. The resultant maximum viscosity of the inner core is 4.23(±0.68)×10^{15} Pa s (Eq. 7). This upper limit of the Earth's inner core viscosity is consistent with a geophysical observation suggesting a viscosity below 3×10^{16} Pa s (Buffett 1997). Considering that typical estimations on the mantle viscosity are in the range of 10^{21} to 10^{24} Pa s, the inner core with a viscosity below 3×10^{16} Pa s would easily accommodate viscous flow. It should be emphasized that the 3×10^{16} Pa s is a result assuming the inner core strain of 0.5, which is a minimum strain for showing deformation induced LPO and if the inner core's viscosity is larger than 3×10^{16} Pa s, seismic anisotropy of the inner core should be explained by mechanisms other than LPO such as shape preferred orientation (for review, see Deguen 2012). The upper bound of viscosity estimated in this study constrains geodynamical mechanisms responsible for the inner core anisotropy. For instance, Lasbleis and Deguen (2015) built regime diagrams of dominant viscous flow in the inner core, and under a given thermal instability regime in the diagram, the dominant viscous flow mechanism is dependent on the viscosity of the inner core. The inner core with a viscosity below 3×10^{16} Pa s suggests that it is likely to be deformed by plume convection under an unstable stratification regime. If the inner core is under a stable stratification regime and the viscosity of the inner core is below 10^{12} Pa s, the azimuthal Lorentz force resulting from the Earth's magnetic field could represent the dominant mechanism. In any case, the Lorentz forces would be significant driving forces of viscous flows, as their effects increase with decreasing viscosity under both the stable and unstable stratification regime (Lasbleis and Deguen 2015).

Frost et al. (2021) recently refined the seismic dataset of the inner core and suggested an inner core viscosity larger than 10^{18} Pa s, which was restricted by their geodynamic model for simulating observed seismic anisotropy of the inner core. In contrast to Frost et al. (2021), we estimated the upper limit of the viscosity more directly from constraints provided by mineral physics. We suggest that further studies are needed to establish plausible geodynamic models capable of explaining both the low viscosity of the inner core and its characteristic seismic features, such as increasing seismic anisotropy with depth or hemispherical dichotomy (Frost et al. 2021; Tanaka and Hamaguchi 1997).

ACKNOWLEDGEMENTS

This study was supported by the Japan Society for the Promotion of Science (JSPS) KAKENHI (grant number 19H00716).

REFERENCES CITED

Akahama, Y., and Kawamura, H. (2006) Pressure calibration of diamond anvil Raman gauge to 310 GPa. Journal of Applied Physics, 100, 043516.

Antonangeli, D., Siebert, J., Badro, J., Farber, D.L., Fiquet, G., Morard, G., and Ryerson, F.J. (2010) Composition of the Earth's inner core from high-pressure sound velocity measurements in Fe–Ni–Si alloys. Earth and Planetary Science Letters, 295, 292–296.

Badro, J., Fiquet, G., Guyot, F., Gregoryanz, E., Occelli, F., Antonangeli, D., and d'Astuto, M. (2007) Effect of light elements on the sound velocities in solid iron: Implications for the composition of Earth's core. Earth and Planetary Science Letters, 254, 233–238.

Blum, W., Eisenlohr, P., and Breutinger, F. (2002) Understanding creep—a review. Metallurgical and Materials Transactions A, 33, 291–303.

Bono, R.K., Tarduno, J.A., Nimmo, F., and Cottrell, R.D. (2019) Young inner core inferred from Ediacaran ultra-low geomagnetic field intensity. Nature Geoscience, 12, 143–147.

Boullier, A.M., and Gueguen, Y. (1975) SP-Mylonites: Origin of some mylonites by superplastic flow. Contributions to Mineralogy and Petrology, 50, 93–104.

Brown, A., and Ashby, M. (1980) Correlations for diffusion constants. Acta Metallurgica, 28, 1085–1101.

Buffett, B.A. (1997) Geodynamic estimates of the viscosity of the Earth's inner core. Nature, 388, 571–573.

Buffett, B.A., and Bloxham, J. (2000) Deformation of Earth's inner core by electromagnetic forces. Geophysical research letters, 27, 4001–4004.

Cormier, V.F., and Li, X. (2002) Frequency-dependent seismic attenuation in the inner core 2. A scattering and fabric interpretation. Journal of Geophysical Research: Solid Earth, 107, ESE 14-11-ESE 14-15.

Crank, J. (1975) The mathematics of diffusion, 414 p. Oxford University Press, New York.

Davies, C.J., Stegman, D.R., and Dumberry, M. (2014) The strength of gravitational core-mantle coupling. Geophysical Research Letters, 41, 3786–3792.

Deguen, R. (2012) Structure and dynamics of Earth's inner core. Earth and Planetary Science Letters, 333-334, 211–225.

Fei, Y., Murphy, C., Shibazaki, Y., Shahar, A., and Huang, H. (2016) Thermal equation of state of hcp-iron: Constraint on the density deficit of Earth's solid inner core. Geophysical Research Letters, 43, 6837–6843.

Fischer, R.A., Campbell, A.J., Reaman, D.M., Miller, N.A., Heinz, D.L., Dera, P., and Prakapenka, V.B. (2013) Phase relations in the Fe–FeSi system at high pressures and temperatures. Earth and Planetary Science Letters, 373, 54–64.

Frost, D.A., Lasbleis, M., Chandler, B., and Romanowicz, B. (2021) Dynamic history of the inner core constrained by seismic anisotropy. Nature Geoscience, 14, 531–535.

Goldstein, J.J., Hanneman, R.E., and Ogilvie, R.G. (1965) Diffusion in the Fe-Ni system at 1 atm and 40 Kbar pressure. Trans. AIME, 233, 812–820.

Harper, J., and Dorn, J.E. (1957) Viscous creep of aluminum near its melting temperature. Acta Metallurgica, 5, 654–665.

Hirose, K., Wood, B., and Vočadlo, L. (2021) Light elements in the Earth's core. Nature Reviews Earth & Environment, 2, 645–658.

Inoue, H., Suehiro, S., Ohta, K., Hirose, K., and Ohishi, Y. (2020) Resistivity saturation of hcp Fe-Si alloys in an internally heated diamond anvil cell: A key to assessing the Earth's core conductivity. Earth and Planetary Science Letters, 543, 116357.

Jackson, I., Gerald, J.D.F., and Kokkonen, H. (2000) High-temperature viscoelastic relaxation in iron and its implications for the shear modulus and attenuation of the Earth's inner core. Journal of Geophysical Research: Solid Earth, 105, 23605–23634.

Jeanloz, R., and Wenk, H.-R. (1988) Convection and anisotropy of the inner core. Geophysical Research Letters, 15, 72–75.

Karato, S.-i. (1999) Seismic anisotropy of the Earth's inner core resulting from flow induced by Maxwell stresses. Nature, 402, 871–873.

Komabayashi, T. (2020) Thermodynamics of the system Fe–Si–O under high pressure and temperature and its implications for Earth's core. Physics and Chemistry of Minerals, 47, 32.

Komabayashi, T., Pesce, G., Morard, G., Antonangeli, D., Sinmyo, R., and Mezouar, M. (2019) Phase transition boundary between fcc and hcp structures in Fe-Si alloy and its implications for terrestrial planetary cores. American Mineralogist, 104, 94–99.

Koot, L., and Dumberry, M. (2011) Viscosity of the Earth's inner core: Constraints from nutation observations. Earth and Planetary Science Letters, 308, 343–349.

Lasbleis, M., and Deguen, R. (2015) Building a regime diagram for the Earth's inner core. Physics of the Earth and Planetary Interiors, 247, 80–93.

Mao, Z., Lin, J.-F., Liu, J., Alatas, A., Gao, L., Zhao, J., and Mao, H.-K. (2012) Sound velocities of Fe and Fe-Si alloy in the Earth's core. Proceedings of the National Academy of Sciences, 109, 10239–10244.

Mehrer, H. (2007) Diffusion in solids: fundamentals, methods, materials, diffusion-controlled processes. Springer Science & Business Media.

Nishihara, Y., Ohuchi, T., Kawazoe, T., Seto, Y., Maruyama, G., Higo, Y., Funakoshi, K.-i., Tange, Y., and Irifune, T. (2018) Deformation-induced crystallographic-preferred orientation of hcp-iron: An experimental study using a deformation-DIA apparatus. Earth and Planetary Science Letters, 490, 151–160.

Ohta, K., Kuwayama, Y., Hirose, K., Shimizu, K., and Ohishi, Y. (2016) Experimental determination of the electrical resistivity of iron at Earth's core conditions. Nature, 534, 95–98.

Olson, P., Deguen, R., Rudolph, M.L., and Zhong, S. (2015) Core evolution driven by mantle global circulation. Physics of the Earth and Planetary Interiors, 243, 44–55.

Poupinet, G., Pillet, R., and Souriau, A. (1983) Possible heterogeneity of the Earth's core deduced from PKIKP travel times. Nature, 305, 204–206.

Reaman, D.M., Colijn, H.O., Yang, F., Hauser, A.J., and Panero, W.R. (2012) Interdiffusion of Earth's core materials to 65 GPa and 2200 K. Earth and Planetary Science Letters, 349, 8–14.

Reaman, D.M., Daehn, G.S., and Panero, W.R. (2011) Predictive mechanism for anisotropy development in the Earth's inner core. Earth and Planetary Science Letters, 312, 437–442.

Ritterbex, S., Tsuchiya, T. (2020) Viscosity of hcp iron at Earth's inner core conditions from density functional theory. Scientific Reports, 10, 1–9.

Romanowicz, B., and Wenk, H.-R. (2017) Anisotropy in the deep Earth. Physics of the Earth and Planetary Interiors, 269, 58–90.

Sakairi, T., Sakamaki, T., Ohtani, E., Fukui, H., Kamada, S., Tsutsui, S., Uchiyama, H., and Baron, A.Q. (2018) Sound velocity measurements of hcp Fe-Si alloy at high pressure and high temperature by inelastic X-ray scattering. American Mineralogist, 103, 85–90.

Sinmyo, R., Hirose, K., and Ohishi, Y. (2019) Melting curve of iron to 290 GPa determined in a resistance-heated diamond-anvil cell. Earth and Planetary Science Letters, 510, 45–52.

Suehiro, S., Wakamatsu, T., Ohta, K., Hirose, K., and Ohishi, Y. (2019) High-temperature electrical resistivity measurements of *hcp* iron to Mbar pressure in an internally resistive heated diamond anvil cell. High Pressure Research, 39, 579–587.

Takehiro, S.-I. (2011) Fluid motions induced by horizontally heterogeneous Joule heating in the Earth's inner core. Physics of the Earth and Planetary Interiors, 184, 134–142.

Tanaka, S., and Hamaguchi, H. (1997) Degree one heterogeneity and hemispherical variation of anisotropy in the inner core from PKP (BC)–PKP (DF) times. Journal of Geophysical Research: Solid Earth, 102, 2925–2938.

Tateno, S., Hirose, K., Ohishi, Y., and Tatsumi, Y. (2010) The Structure of Iron in Earth's Inner Core. Science, 330, 359–361.

Tateno, S., Kuwayama, Y., Hirose, K., and Ohishi, Y. (2015) The structure of Fe–Si alloy in Earth's inner core. Earth and Planetary Science Letters, 418, 11–19.

Tsujino, N., Nishihara, Y., Nakajima, Y., Takahashi, E., Funakoshi, K.-i., and Higo, Y. (2013) Equation of state of γ-Fe: Reference density for planetary cores. Earth and Planetary Science Letters, 375, 244–253.

Van Orman, J.A. (2004) On the viscosity and creep mechanism of Earth's inner core. Geophysical Research Letters, 31, L20606.

Vočadlo, L., Dobson, D.P., and Wood, I.G. (2009) *Ab initio* calculations of the elasticity of hcp-Fe as a function of temperature at inner-core pressure. Earth and Planetary Science Letters, 288, 534–538.

Weertman, J. (1957) Steady-State Creep through Dislocation Climb. Journal of Applied Physics, 28, 362–364.

Yamazaki, D., Tsujino, N., Yoneda, A., Ito, E., Yoshino, T., Tange, Y., and Higo, Y. (2017) Grain growth of ε-iron: Implications to grain size and its evolution in the Earth's inner core. Earth and Planetary Science Letters, 459, 238–243.

Yoshida, S., Sumita, I., and Kumazawa, M. (1996) Growth model of the inner core coupled with the outer core dynamics and the resulting elastic anisotropy. Journal of Geophysical Research: Solid Earth, 101, 28085–28103.

Yunker, M.L., and Van Orman, J.A. (2007) Interdiffusion of solid iron and nickel at high pressure. Earth and Planetary Science Letters, 254, 203–213.

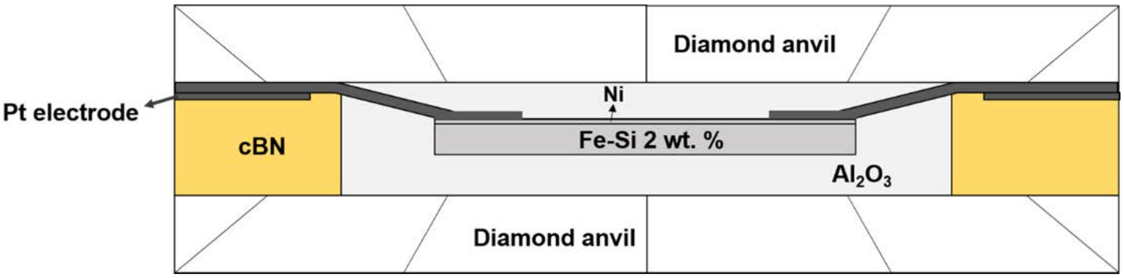

FIGURE 1. Schematic illustration of sample configuration of an internal-resistive-heated DAC.

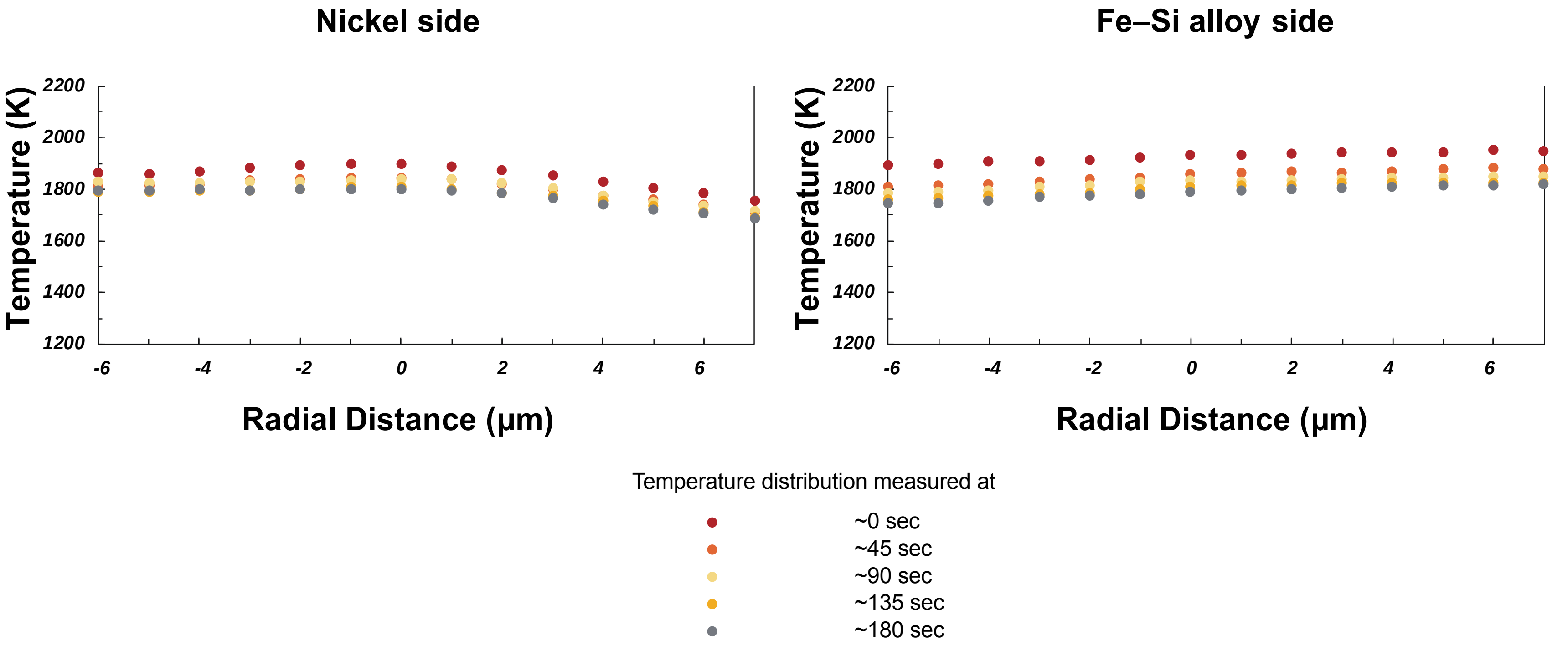

FIGURE 2. Temperature profiles of a representative specimen during a diffusion experiment (Run #1). The lateral extent of each temperature point is 0.5 μm to the left and right.

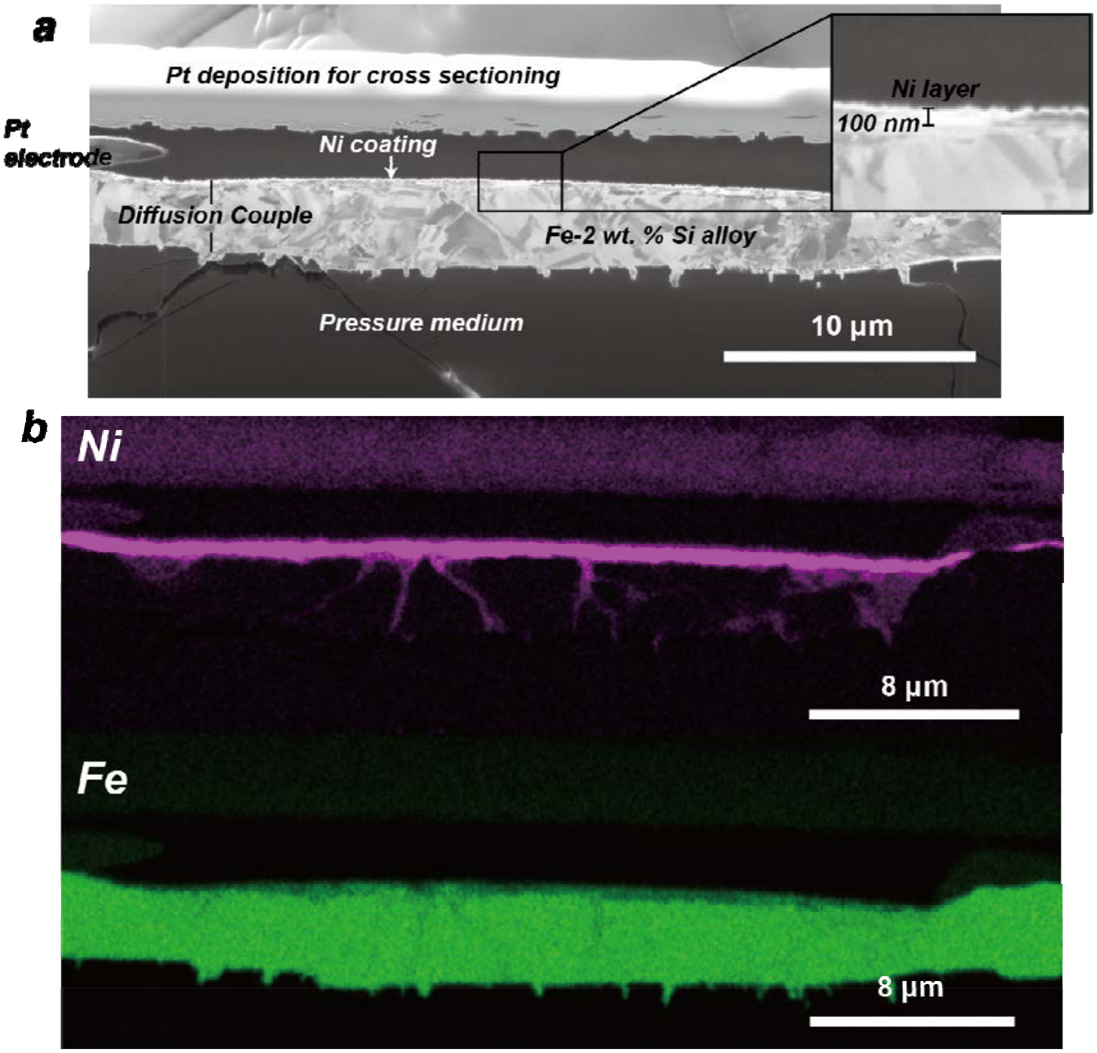

FIGURE 3. (a) SIM image, and (b) SEM-EDS mapping images of sample cross section (run #3). The inset (a) shows enlarged view of boundary between Ni layer and Fe–2 wt.% Si alloy.

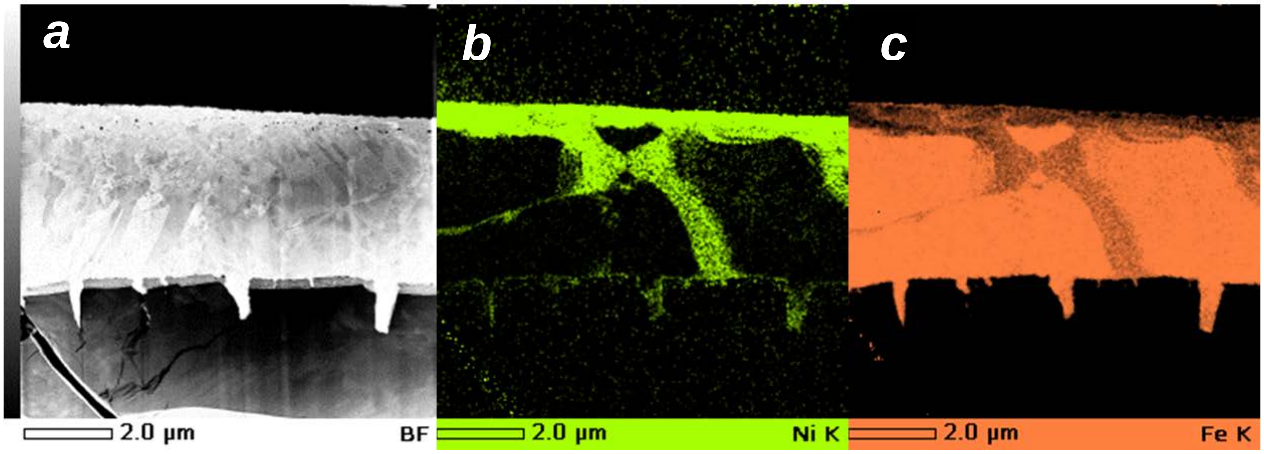

FIGURE 4. (a) TEM bright field image (run #3). (b), (c) Corresponding TEM-EDS mapping images of Ni and Fe.

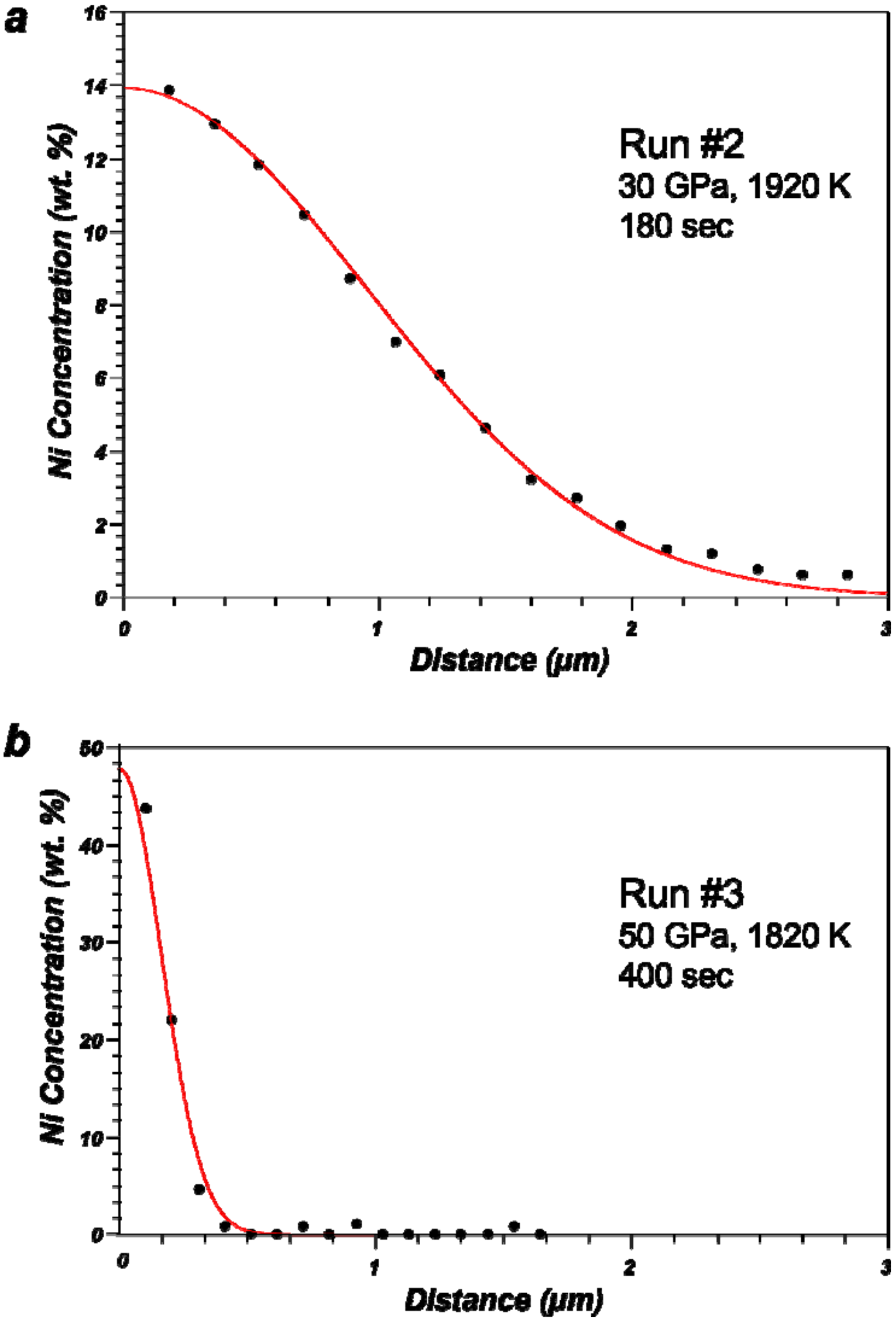

FIGURE 5. Representative diffusion profiles of Ni obtained by TEM-EDS analyses after diffusion experiments at temperature and pressure conditions of (a) ~1920 K, ~30 GPa, and (b) ~1820 K, ~50 GPa. The measurement error for Ni concentration is less than 2%. The distance uncertainty is about 1.0 nm, which corresponds to the diameter of the EDS electron probe. Red curves indicate best fitting curves of the thin film solution to the measured diffusion profiles.

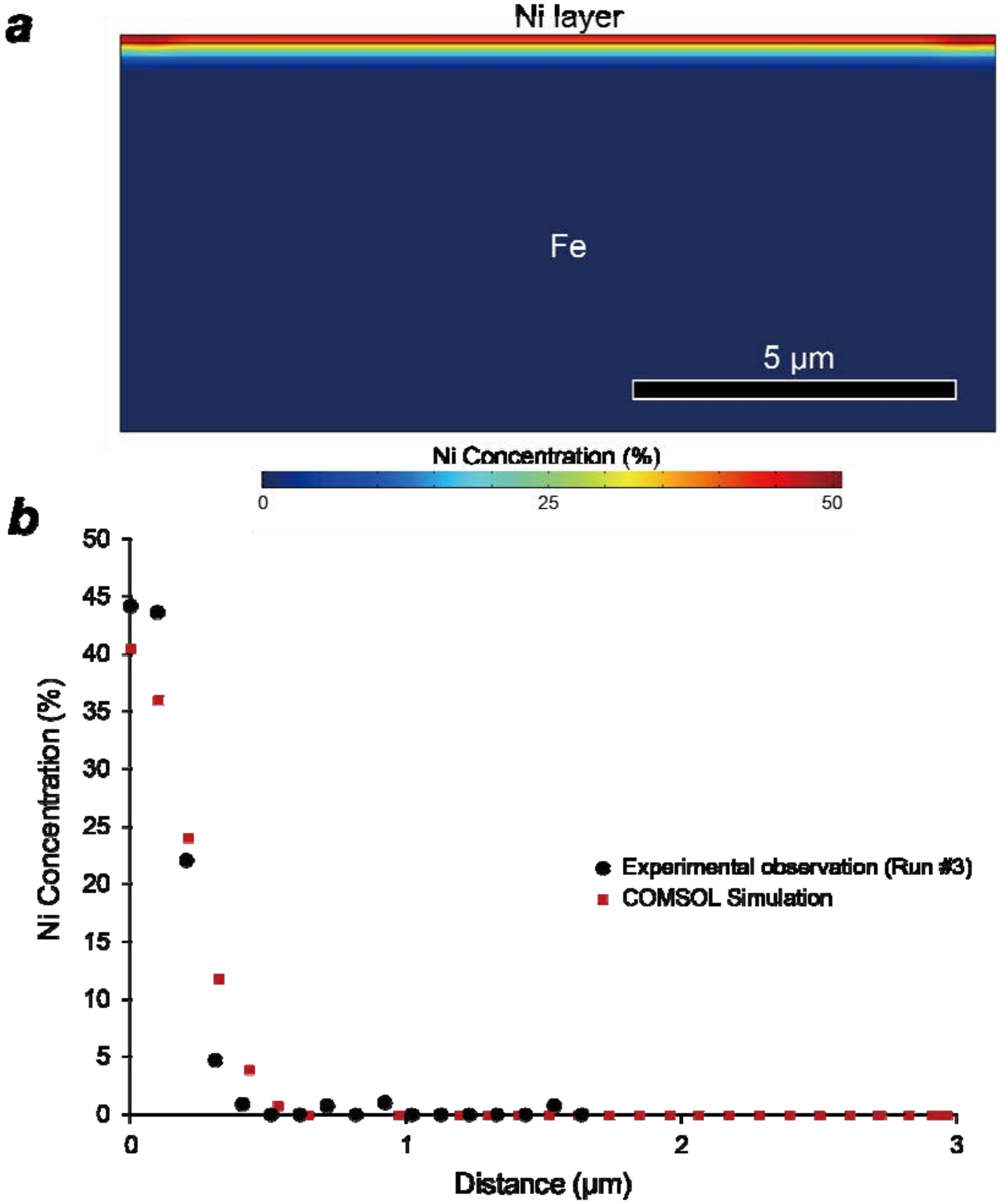

FIGURE 6. (a) A result of COMSOL simulation assuming diffusion tracer thickness of 120 nm and diffusion coefficient of 4.08×10^{-17} m^2 s^{-1} obtained by fitting the diffusion profile of Run #3 to the thin film solution. (b) Comparison of diffusion profiles from an actual experimental observation (Run #3) and the COMSOL simulation. The measurement error for Ni concentration is less than 2%. The distance uncertainty is about 1.0 nm, which corresponds to the diameter of the EDS electron probe.

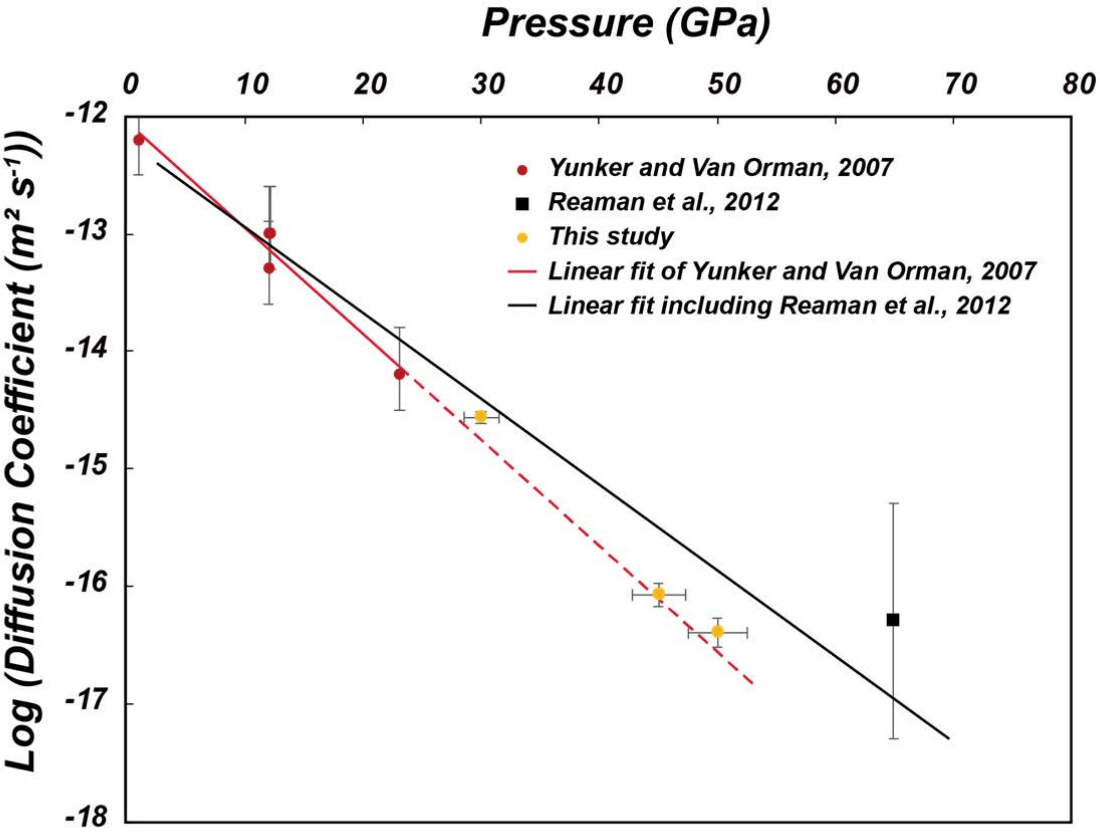

FIGURE 7. Diffusion coefficients against pressure under similar temperature conditions. Temperature conditions are in a range from ~1800 to ~1900 K. Red dots and a black dot indicate Fe–Ni interdiffusion coefficients from Yunker and Van Orman (2007) and Reaman et al. (2012), respectively, without considering silicon.

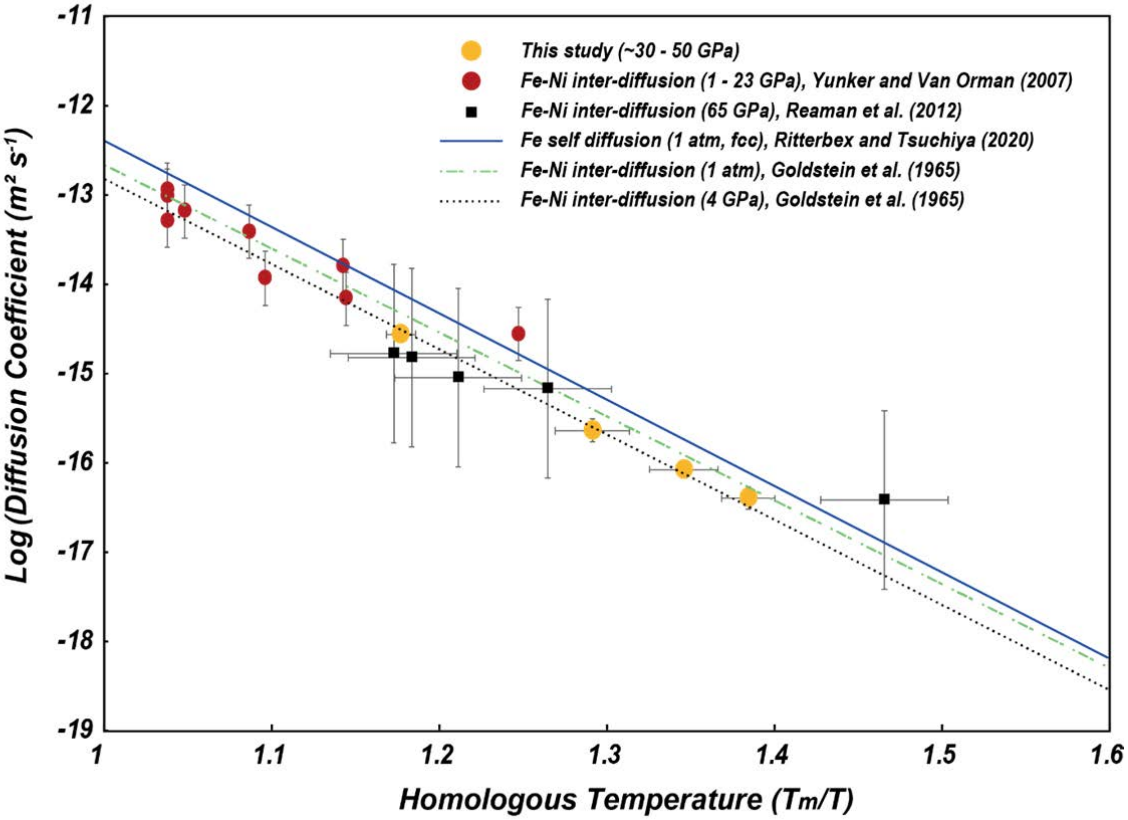

FIGURE 8. Diffusion coefficients in this study versus homologous temperature and previous results of Fe–Ni interdiffusion experiments under various pressure ranges (1 atm to 65 GPa, Goldstein et al. 1965; Yunker and Van Orman 2007; Reaman et al. 2012) and Fe self-diffusion coefficients in fcc Fe under atmospheric pressure estimated from density functional theory calculations (Ritterbex and Tsuchiya 2020).

TABLE 1. Summary of diffusion experiments conducted in this study

Run #	Pressure (GPa)	Temperature (K)	Diffusion time (s)	Diffusion coefficient (m^2 s^{-1})
#1	45 (±2)	1820 (±50)	180	8.52×10^{-17} ($\pm1.14\times10^{-17}$)
#2	30 (±2)	1920 (±20)	180	2.74×10^{-15} ($\pm1.85\times10^{-16}$)
#3	50 (±3)	1820 (±40)	400	4.08×10^{-17} ($\pm8.18\times10^{-18}$)
#4	31 (±2)	1750 (±50)	250	2.37×10^{-16} ($\pm7.12\times10^{-17}$)